Journal of Materials Research and Technology 34 (2025) 807–818

Contents lists available at ScienceDirect

Journal of Materials Research and Technology

journal homepage: www.elsevier.com/locate/jmrt

Preparing strong and ductile AZ80 Mg alloy via warm rotary swaging

Zhenghao Li [a], Mengning Xu [a], Kaixuan Zhou [a], Yang Cao [a,b,**], Yonghao Zhao [a,b,*]

[a] Nano and Heterogeneous Materials Center, School of Materials Science and Engineering, Nanjing University of Science and Technology, Nanjing, 210094, China
[b] School of Materials Science and Engineering, Hohai University, Changzhou, 213200, China

ARTICLE INFO

Handling Editor: L Murr

Keywords:
Magnesium alloy
Plastic deformation
Precipitation
Heterostructure
Nano-structure

ABSTRACT

Rotary swaging at different temperatures has been conducted to process the AZ80 Mg alloy rods, and the results are compared. Rotary swaging to an equivalent strain of 0.25 at room temperature, induced high densities of deformation twins and macrocracks, causing catastrophic failure of the swaged rods. In contrast, repetitive conduct of 260°C-swaging and water cooling promotes <c + a> dislocation slip and localized grain refinement via twinning and dynamic recrystallization, and thus to lower the number of large twin bands in coarse grains. The sample processed by 260°C-swaging and water cooling has a nano-structural hierarchy consisting of bimodal grain size distributions and high densities of nano-precipitates located at grain boundaries of the ultrafine grains and at coarse-grain interiors, and shows a gradient hardness distribution from the periphery to center of the rod; Correspondingly, the 260 °C swaged sample shows outstanding combinations of strength and ductility at both the peripheral and central regions.

1. Introduction

Magnesium alloys are considered as one of the most promising green engineering materials in the new era, because of the excellent combination of properties including low density, high specific strength, good damping capacity and good electromagnetic shielding capability. Moreover, they are recyclable and resource-abundant [1,2]. Therefore, researchers and engineers are keen to expand the applications of Mg alloys in many fields of industries, such as automobiles, high-speed railways, aerospace vehicles, electronic communication, etc. However, compared with other light-weight structural materials such as Al and Ti alloys, Mg alloys still have shortcomings including low strength, fracture toughness [3], ductility [4] and corrosion resistance [5]. Mg alloys have a hexagonal close-packed (HCP) atomic structure with an insufficient number of easy-slip systems. The critical resolved shear stress (CRSS) for basal slip is low, but the CRSSs for non-basal slip systems, such as $\{10\,\bar{1}\,0\}$ prismatic and $\{11\bar{2}\,2\}$ pyramidal slip systems (<c> and <c + a> slip), are much higher [6]. Therefore, coarse grained Mg alloys tend to fracture at low tensile stresses, rendering the low ductility and formability [7,8]. In this context, enhancing the strength and ductility of Mg alloys is a key issue in the industrial application.

Mg alloys can be strengthened via solid solution [9], precipitation [10] and grain refinement [11]. Kula et al. [12] have done systematic research work to reveal the importance of Gd and Y in Mg–Gd and Mg–Y solid solutions for altering strain rate sensitivities and thus the ductility. Fan et al. [13] showed that by controlling the contents of Er, Y and Zn in cast Mg alloys, precipitation strengthening and <c + a> dislocations can be effectively stimulated for strength-ductility synergy. Xu et al. [14] carried out high quality in-situ transmission electron microscopy (TEM) analysis to capture the details of Orowan type dislocation-β' phase interactions in aged Mg–Gd alloys, revealing the underlying physics of precipitation strengthening. Although, solid solution and precipitation strengthening have been proven effective for making high strength Mg alloys, their effectiveness are intrinsically limited by the solubilities of alloying elements and brittleness of precipitates.

Grain refinement to the lower bound of the micrometer range is also a promising approach that can simultaneously improve the strength and ductility of Mg alloys. Liu et al. [15] processed a Mg–10Gd–6Y–1.5Zn–0.5Zr alloy with an average grain size of ~1 μm and excellent mechanical properties by the equal-channel angular pressing (ECAP) method. Both Wei et al. [16] and Luo et al. [17] have reported that <c + a> dislocations prevail over twinning and <a>

* Corresponding author. Nano and Heterogeneous Materials Center, School of Materials Science and Engineering, Nanjing University of Science and Technology, Nanjing, 210094, China.
** Corresponding author. Nano and Heterogeneous Materials Center, School of Materials Science and Engineering, Nanjing University of Science and Technology, Nanjing, 210094, China.
E-mail addresses: y.cao@njust.edu.cn (Y. Cao), yhzhao@njust.edu.cn (Y. Zhao).

https://doi.org/10.1016/j.jmrt.2024.12.079
Received 1 November 2024; Received in revised form 8 December 2024; Accepted 10 December 2024
Available online 11 December 2024

dislocations in grains with the sizes smaller than ~5 μm; Therefore, fine-grained Mg alloys usually show excellent strengths and ductility. However, grain refinement to the ultrafine-grained regime or even nanocrystalline regime, would face various challenges including dynamic recrystallization, high power consumption, and sample size limitation [18–20]. Nevertheless, different from coarse grained Mg alloys, homogeneous ultrafine grains (UFGs) and nanograins grants the Mg alloys with ultrahigh strength at the expense of ductility [21].

Heterostructured materials which unites the high strength of nanostructures and high ductility of coarse-grained structures, have recently gained tremendous attentions from the materials science community [22–24]. Zha et al. [25] made heterostructured WE43 alloy which is constituted of bimodal grain size distributions. Fan et al. [26] produced a heterostructured $Ni_{42}Fe_{30}Cr_{12}Mn_8Al_5Ti_3$ alloy that is constituted of $L1_2$ nanoprecipitates hardened fine and ultrafine recrystallized grains, showing ultrahigh strength of 1.8 GPa and a remarkable uniform elongation of 18.2%. Nie et al. [27] produced a dual-heterostructured aluminum matrix composite that demonstrating dual level hetero-deformation induced (HDI) strengthening effect to improve the strength-ductility synergy for the intrinsically brittle composite.

The above-mentioned results provide the guidance for microstructures and mechanical properties optimizations in Mg alloys. Nevertheless, the choice of appropriate materials processing techniques is another equally vital issue. Recently, several bulk high-strength Mg alloys have been successfully fabricated by means of rotary swaging (RS) at high strain rates and low deformation strains. For example, Wan et al. [28] have produced a bulk nanocrystalline Mg–Gd–Y–Zr alloy with an average grain size of ~80 nm and record-breaking high strength of 710 MPa by the RS method. Cui et al. [29] used the RS method to process the heterostructured Mg–6Li–3Al–0.4Ce alloy with a high strength of 411 MPa, uniform elongation of 11 % and specific strength of 258 $kN{\cdot}m{\cdot}kg^{-1}$. RS is a mature industrial method with low cost and simple setup, and it is capable of processing rod, tubes and bar of unlimited lengths [30–32]. However, the complex three-dimensional stress/strain states imposed by RS usually result in the formation of complex microstructures which in turn alter the mechanical properties of the processed materials in wide ranges [33–35]. Although RS is proven a promising method, there are only a few studies on the microstructure and mechanical properties of Mg alloys prepared by RS.

In this work, RS at room temperature and elevated temperature have been done in seek of mechanical properties optimization in an AZ80 Mg alloy. Knowing that the mechanical properties of metallic materials may scatter in a wide range in accordance to the widely adjustable heterostructures [22,24,25], this work has relied upon the selection of heterostructures to optimize the strength and ductility combination in the AZ80 Mg alloy. We successfully prepared strong and ductile AZ80 Mg alloy samples via a nano-structural hierarchy strategy, and revealed the potential deformation mechanisms through multi-scale microstructure characterization. This work provides insights for the fabrication of Mg alloys with strength-ductility synergy by plastic deformation.

2. Experimental procedures

2.1. Sample preparation

An as-extruded AZ80 Mg alloy rod with the initial diameter of 20 mm was employed as the starting material. The chemical composition of the as-received material is listed in Table 1.

Fig. 1a shows the principal setup of RS. The four dies were placed around the rod. During RS, the dies revolve at a high angular speed, and simultaneously impose high-frequency short-distance impacts along the radial direction of the rod. The equivalent strain imposed by RS is $\varepsilon = \ln(S_0/S_1)$, where S_0 and S_1 are the initial and final cross-sectional areas, respectively. It is noteworthy that the strain imposed by each pass should be small, to avoid microscopic and macroscopic cracks caused by stress concentration and non-uniform deformation. Two different RS processing routes were used to alter the microstructure and thus to improve the strength of the AZ80 alloy. In route one, an as-received rod was subjected to multi-pass RS at room temperature to a final diameter of ~17.7 mm. The resultant cross-sectional area reduction was 21.7%, and the total equivalent strain was ~0.25. The sample processed by route one is termed the RT-0.25 sample. In route two, an as-received rod was preheated at 260 °C for 10 min, then immediately processed through RS and subsequent water-cooling. The preheating-RS-cooling procedure was repeated several times to process the rod to a diameter of ~14.1 mm. The cross-sectional area reduction by route two was 50.3%, and the equivalent strain was ~0.70. The processed sample is termed the 260°C-0.70 sample. Fig. 1b shows the as-received and RS processed samples. When the AZ80 Mg alloy rod was RS processed to an equivalent strain of 0.25 at room temperature, the rod cracked into several pieces. In contrast, the AZ80 Mg alloy rod can be swaged at 260 °C to a strain of 0.7 without cracks.

Table 1
Chemical composition of the as-received AZ80 alloy.

Element	Mg	Al	Zn	Mn	Si	Fe
Weight percent	Bal.	7.640	0.580	0.210	0.012	0.015

2.2. Mechanical properties tests

As illustrated in Fig. 1c, the feeding direction for RS is parallel to the axial direction (AD) of the rod. Hardness tests and microstructural characterization have been done on planes perpendicular to AD and radial direction (RD).

Samples were sliced from the rods and mechanically polished to mirror finish prior to hardness tests. Vickers micro-hardness tests were performed using an HMV-G 21 DT (Shimadzu, Japan) tester with a load of 2.94 N and a dwell time of 15 s. Uniaxial tensile tests were performed using a LFM 20 kN (walter + bai, Switzerland) tester with a constant strain rate of $1 \times 10^{-3}\ s^{-1}$ at room temperature. Flat dog-bone shaped tensile specimens with a gauge length of 10 mm and a transverse section of $1.5 \times 2.5\ mm^2$ were sectioned by wire electrical discharge machining from the rods with the long gauge axis parallel to the AD.

2.3. Microstructural characterization

Microstructural analyses were performed by means of X-ray diffraction (XRD), optical microscopy (OM), scanning electron microscopy (SEM), electron backscatter diffraction (EBSD), TEM and high-resolution transmission electron microscopy (HRTEM).

Samples for XRD, OM, SEM and EBSD analysis were prepared by mechanical polishing to mirror finish. In order to reveal grain boundaries (GBs) under OM, the polished sample was etched in the solution of 4 ml nitric acid and 96 ml alcohol. Macroscopic phase identification by XRD was performed using a Bruker-AXS D8 Advance X-ray diffractometer with Cu-Kα radiation at 40 kV and 40 mA. Olympus BX41M microscope was used for OM imaging. SEM observations were carried out on the FEI Quanta 250F microscope equipped with an Oxford energy dispersive spectrometer (EDS). EBSD analysis was carried out on a Zeiss Auriga field-emission SEM equipped with an Oxford EBSD detector. Mechanically polished samples were electropolished in a commercial polishing solution AC-2 at 20 V and −30 °C for 150 s prior to EBSD analysis.

TECNAI G2 20 LaB6 TEM with an acceleration voltage of 200 kV was used to obtain bright-field images and diffraction patterns. HRTEM was performed on an FEI Titan G2 60-300 aberration-corrected TEM operating at 300 kV. TEM foils were sliced by wire electrical discharge machining and mechanically polished to a final thickness of about 30 μm. Perforation of foils was done on a Gatan PIPS 691 ion milling machine with a low energy of 4 KeV and a low angle of 3°.

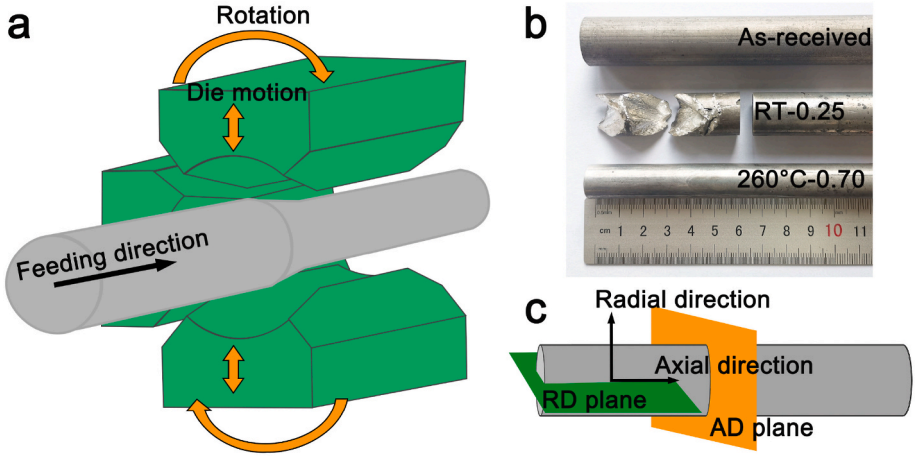

Fig. 1. (a) Schematic diagram of RS. (b) The rotary swaged alloys rods. (c) Sectioning of alloy rods for microstructural analysis.

3. Results

3.1. Mechanical properties

Fig. 2 shows the microhardness of as-received, RT-0.25 and 260°C-0.70 samples measured along radial directions of the rod on AD and RD planes. The microhardness of as-received samples is low and uniformly distributed throughout the entire sample. The microhardness of the RT-0.25 and 260°C-0.70 samples are similar, and show V-shape distributions with the hardness of ~95 HV at the center and gradually increases to 110 HV at the periphery.

Dog-bone-shaped specimens were taken from the center and at the radial distance of 5 mm from the center for tensile tests. The engineering stress-strain curves are shown in Fig. 3a. Both the 260°C-0.70-periphery and 260°C-0.70-center samples show excellent combinations of strength and ductility. The 260°C-0.70-center sample has a yield strength (YS), ultimate tensile strength (UTS), uniform elongation (UL) and elongation to failure (EL) of 363 MPa, 427 MPa, 7.0%, 8.6%, respectively. The 260°C-0.70-periphery sample is even better, shows a YS, UTS, UL and EL of 388 MPa, 471 MPa, 8.2% and 8.9%, respectively. Apparently, RS processing at 260 °C has significantly improved the strength of the materials without sacrificing much of the ductility. In contrast, the samples processed by RS at room temperature has lost too much ductility, e.g. both the RT-0.25-periphery and RT-0.25-center samples have very low ductility below 2.5%. It is noteworthy that the YS of the RT-0.25-periphery and RT-0.25-center samples are nearly identical to the YS of 260°C-0.70-periphery and 260°C-0.70-center samples, respectively. Table 2 summarizes mechanical properties of the AZ80 alloys for the reader's convenience. Fig. 3b compares the UTS and ductility of the 260°C-0.70-periphery and 260°C-0.70-center samples with the data from literatures, indicating that RS processing at 260 °C is capable of optimizing the mechanical properties of an AZ80 alloy.

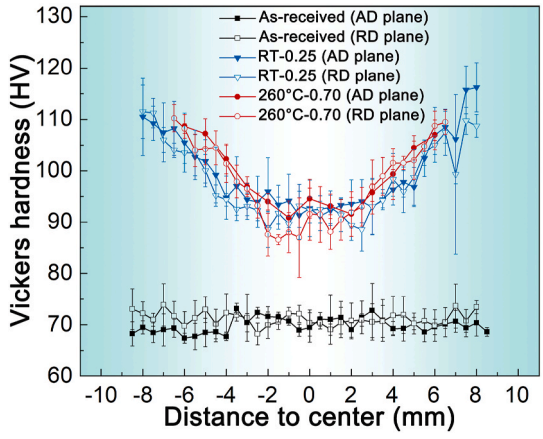

Fig. 2. Vickers micro-hardness measured along the radial directions on AD and RD planes of the AZ80 alloy rods.

3.2. Microstructure of the as-received AZ80 alloy

The as-received AZ80 alloy has equiaxed coarse-grains (CGs) (Fig. 4a) with an average grain size of 24.2 μm (Fig. 4b). XRD pattern, in Fig. 4c, shows that there are α-Mg and β-$Mg_{17}Al_{12}$ phases in the as-received AZ80 alloy. Fig. 4d is a TEM image showing spherical nano-precipitates randomly distributed within a grain. Fig. 5a–d shows nearly identical equiaxed CGs viewed at periphery and center of the rod on AD and RD planes, and thus confirm that the as-received AZ80 alloy has homogeneous distribution of equiaxed CGs throughout the entire sample. Precipitates agglomerate along GBs to form precipitate-networks. Typical discontinuous precipitation of β-$Mg_{17}Al_{12}$ phase occurred randomly as shown in Fig. 5d; The precipitate nucleated at the GB and grew into the grain interior. There are also a few micro-size polygonal particles observed in Fig. 5a. XRD mapping in Fig. 5e confirms that the micro-size polygonal particles are the Al_8Mn_5 intermetallic compound which is the minor impurity formed during casting [37, 44].

3.3. Microstructures of RS AZ80 alloys

While the RS samples show different mechanical properties at the peripheral and central regions, as show in Figs. 2 and 3, the microstructures at the peripheral and central regions are analyzed in detail to seek for the scientific explanation. As shown in Fig. 6, there is no significant change to the shapes of the precipitate-networks in the RT-0.25 sample. However, it is noteworthy that the precipitate-networks observed on the RD planes (Fig. 6b and d) are stretched a little more in the AD direction (vertical direction) than that observed on the AD planes (Fig. 6a and c). A chunk of Al_8Mn_5 intermetallic compound has been broken into four pieces and ripped apart in the AD direction as shown in Fig. 6b. Thus, the plastic flow in the AD direction seems stronger than in the RD direction. Although, the equivalent strain was only 0.25, there has already been some cavities or voids formed in the RT-0.25 sample, as shown in Fig. 6c. Therefore, the AZ80 alloy has a poor formability and plasticity under the room temperature RS processing condition.

RS at elevated temperatures such as 260 °C can impose much higher strain than room temperature RS without cracks. As shown in Fig. 7, cavities or voids are hardly seen in the 260°C-0.70 sample. At the

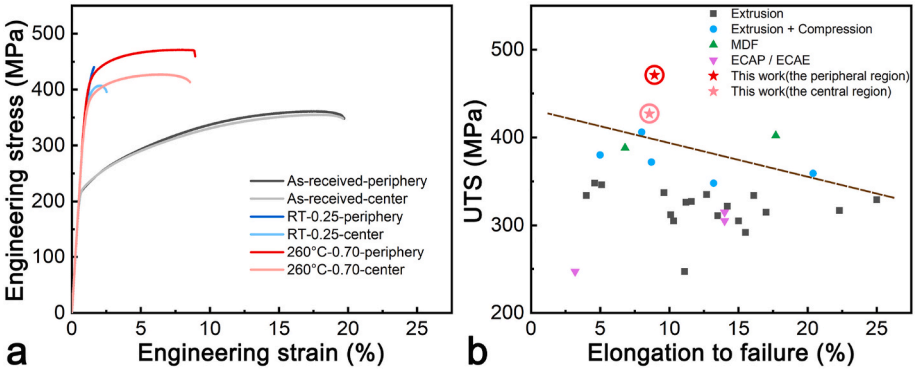

Fig. 3. Tensile properties of the AZ80 alloy specimens: (a) Engineering stress-strain curves; (b) Comparison for tensile properties of AZ80 alloys [36–50].

Table 2
Mechanical properties of the AZ80 alloy processed under different conditions.

Sample	YS, MPa	UTS, MPa	UL, %	EL, %
As-received-periphery	217	361	18.2	19.7
As-received-center	213	355	18.6	19.6
RT-0.25-periphery	383	440	1.6	1.6
RT-0.25-center	359	407	2.2	2.5
260°C-0.70-periphery	388	471	8.2	8.9
260°C-0.70-center	363	427	7.0	8.6

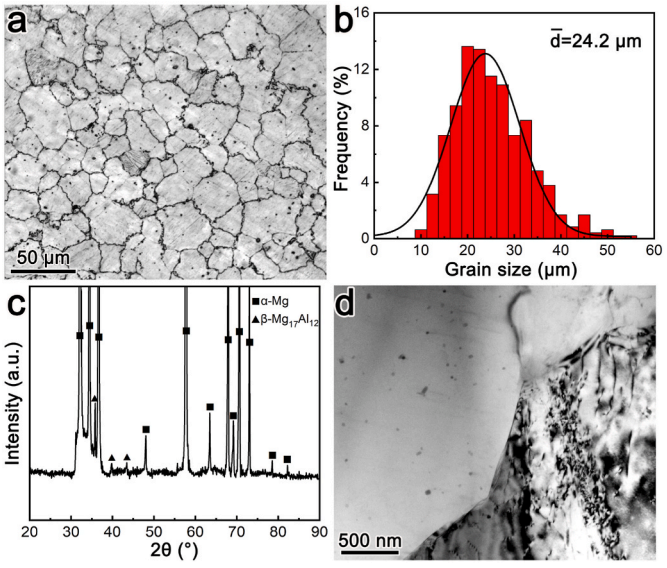

Fig. 4. Microstructure and phase contents in the as-received AZ80 alloy rod: (a) An optical micrograph showing grains on the AD plane; (b) A histogram of grain size distribution; (c) The XRD pattern; (d) A bright-field TEM image showing microstructures viewed on the AD plane.

peripheral region on the AD plane, the precipitate-network is hardly observable, instead, very fine precipitates are homogeneously distributed with a high density throughout the entire field of view, as shown in Fig. 7a. As shown in Fig. 7b, for the same peripheral region but viewed on the RD plane, the precipitate-networks are still observable, but stretched severely in the AD direction; In addition, there are dense dispersions of fine precipitates in many local areas. Precipitate-networks are still seen in the central region when viewed on both AD and RD planes, as shown in Fig. 7c and d, respectively. However, dense dispersions of fine precipitates in local areas are seen on both planes. Again, the precipitate-network is stretched more on the RD plane than AD plane. The reshaping of networks and redistribution of precipitates are done by the strong plastic flow and dislocation activities. Similar strain induced redistribution of precipitates is also observed in ECAP deformation of AZ80 alloy by Tang et al. [44].

Discontinuous and continuous β-$Mg_{17}Al_{12}$ precipitates are seen in the same region in the 260°C-0.70 sample, as shown in Fig. 8a. The thickness, length and lamellar spacing of the discontinuous precipitates are ~125 nm, 0.73–4.90 μm, and ~366 nm, respectively. In contrast, the average size of continuous precipitates at GBs is ~165 nm only, while the sizes of the continuous precipitates at grain interiors are even smaller, as shown in Fig. 8b. Discontinuous and continuous precipitation competes for nucleation and growth [51]. Apparently, continuous precipitation has inhibited discontinuous precipitation, therefore only a small number of discontinuous precipitates are seen randomly at interfaces where the stored energy is high due to accumulation of dislocations [52].

The RT-0.25 sample preserved the shapes of the original CGs, but inside the CGs there are many deformation twins as shown in Fig. 9a and b. The density of deformation twins at the periphery is higher than at the center. Moreover, the EBSD hit-rate at the periphery is significantly lower than at the center, as shown in Fig. 9a and b, indicating that the defect densities are higher at the periphery. Significant grain refinement has been achieved at the periphery of the 260°C-0.70 sample, resulting in the bimodal grain size distribution, as shown in Fig. 9c. UFGs agglomerate into "necklace" structures to subdivide the CGs. In contrast, the microstructure at the center of the 260°C-0.70 sample is like the intermediate state between as-received sample and the periphery of the 260°C-0.70 sample, as shown in Fig. 9d; The shapes of the original CGs are still identifiable, but some thin deformation bands containing UFGs have already formed inside the CGs.

As shown in Fig. 10a1 and a2, at the periphery of the RT-0.25 sample, the fractions of low angle grain boundaries (LAGBs), 86.3° {10 $\bar{1}$ 2} twin boundaries (TBs) and 38° {10 $\bar{1}$ 1}–{10 $\bar{1}$ 2} TBs are 74.8%, 8.21% and 0.78%, respectively. As shown in Fig. 10b1 and b2, at the center of the RT-0.25 sample, the fractions of LAGBs, 86.3° {10 $\bar{1}$ 2} TBs, 38° {10 $\bar{1}$ 1}–{10 $\bar{1}$ 2} TBs and 56.2° {10 $\bar{1}$ 1} TBs are 73.9%, 2.22%, 3.63% and 1.28%, respectively. The very high fractions of LAGBs and the peaks for TB fractions in Fig. 10a2 and b2, indicate that both dislocations and twins are the major carriers for plastic strain. In contrast, the fractions of LAGBs at the periphery and center of the 260°C-0.70 sample have decreased to 62.9% and 71.4%, respectively, as shown in Fig. 10c2 and d2. Although the statistical data in Fig. 10c2 and d2 show that the fractions of 86.3° {10 $\bar{1}$ 2} TBs are still above 6%, long and straight coherent TBs are hardly seen in the EBSD maps shown in Fig. 10c1 and d1. Therefore, the TBs are in fact fragments of TBs that form as a part of the dynamic recrystallization (DRX) process [53]. In addition, the peaks at 30° in the misorientation distribution histograms in Fig. 10c2 and d2 are also the evidence for DRX. The 30° [0001] GBs have lower interfacial energies and higher mobility than other GBs, thus they are more likely to become the growth sites for the DRX [54].

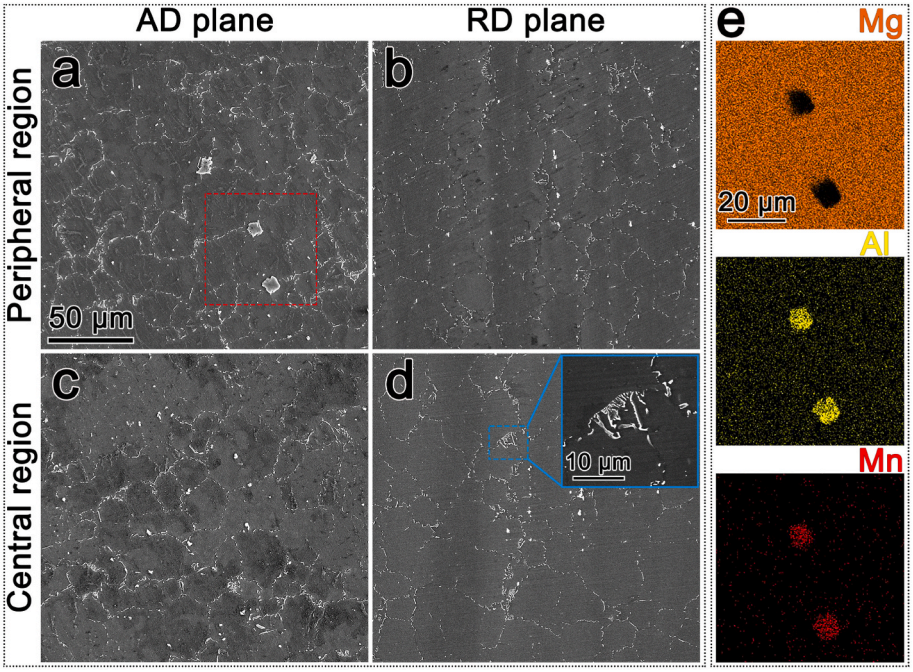

Fig. 5. SEM images of the as-received sample: The peripheral region observed on (a) AD and (b) RD planes; The central region observed on (c) AD and (d) RD planes; The inset in (d) is a high-magnification image of typical β-$Mg_{17}Al_{12}$ phase formed by discontinuous precipitation. (e) EDS maps showing elemental distributions and Al_8Mn_5 particles in the area enclosed by a red square in (a).

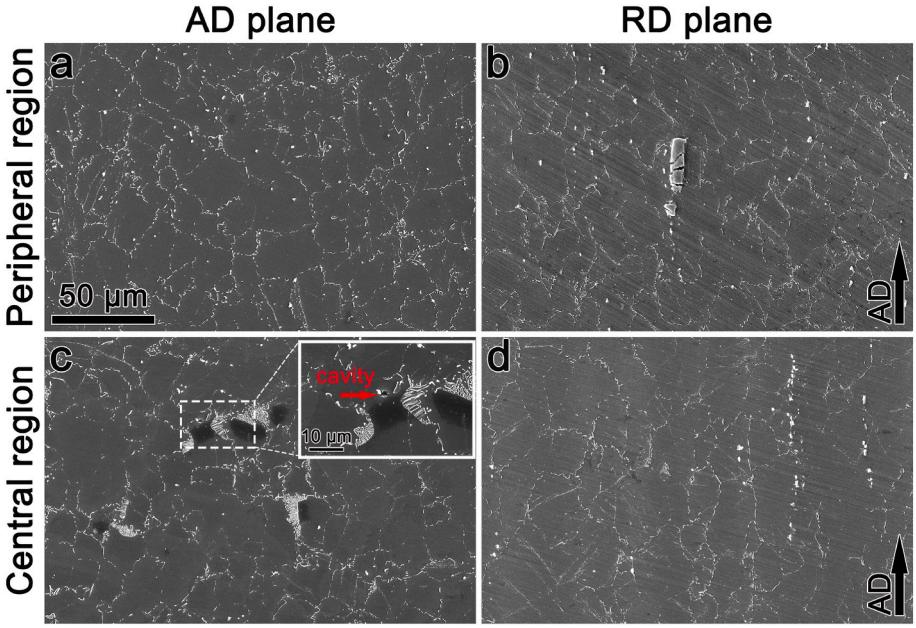

Fig. 6. SEM images of the RT-0.25 sample: The peripheral region observed from (a) AD and (b) RD planes; The central region observed from (c) AD and (d) RD planes; The inset in (c) is high-magnification image showing cavity and β-$Mg_{17}Al_{12}$ precipitates.

The EBSD hit-rates were low in Figs. 9 and 10, due to the presence of high densities of defects. In order to resolve the defects in the RS AZ80 Mg alloy rods, detailed TEM analysis has been carried out. As shown in Fig. 11a, there are very high densities of deformation twins in the periphery of the RT-0.25 sample. Based on the difference in contrast, the original CGs can be identified, although the GBs delineated by red dashed-lines were faintly visible due to the strong plastic strain in the local area. HRTEM at the [1 $\bar{2}$ 10] zone axis confirms that the majority of the twin bands are 86.3° {10 $\bar{1}$ 2} tension twins as shown in Fig. 11b. However, a significant number of the 86.3° {10 $\bar{1}$ 2} tension twins have deviated away from the original 86.3° misorientation. As shown in Fig. 11b, there is a high density of stacking faults (SFs) parallel to the basal planes. As shown in Fig. 11c, the twin boundary has lost the coherency and created a misorientation angle of 89.4°. Apparently, the 86.3° {10 $\bar{1}$ 2} twinning has re-oriented the twinned area to favor basal slip [53], and the pronounced basal slip inclined to the coherent {10 $\bar{1}$ 2} TB has destroyed the coherency. Thus, the actual twin densities and dislocation densities in the periphery of the RT-0.25 sample is much higher than that shown in the EBSD maps in Figs. 9a and 10a1.

The twin density at the center of the RT-0.25 sample is much lower

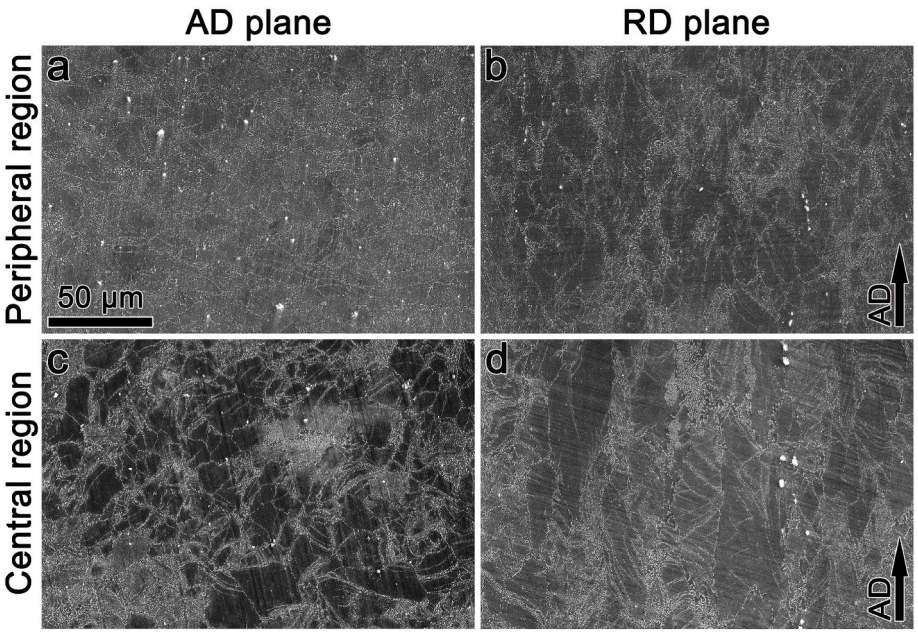

Fig. 7. SEM images of the 260°C-0.70 sample: The peripheral region observed from (a) AD and (b) RD planes; The central region observed from (c) AD and (d) RD planes.

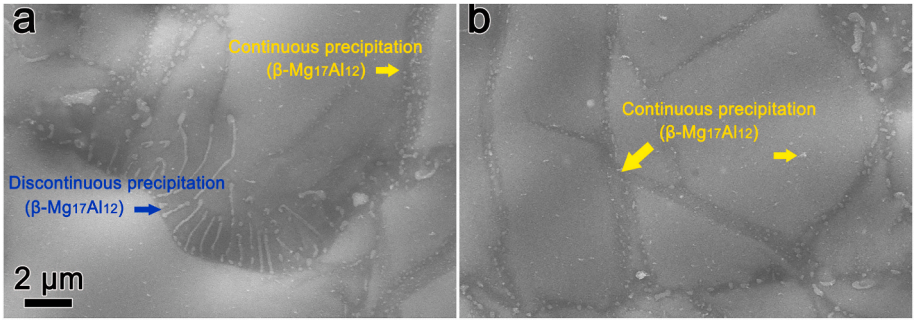

Fig. 8. SEM images showing (a) discontinuous β-$Mg_{17}Al_{12}$ precipitates and (b) continuous β-$Mg_{17}Al_{12}$ precipitates in the 260°C-0.70 sample viewed from the AD plane.

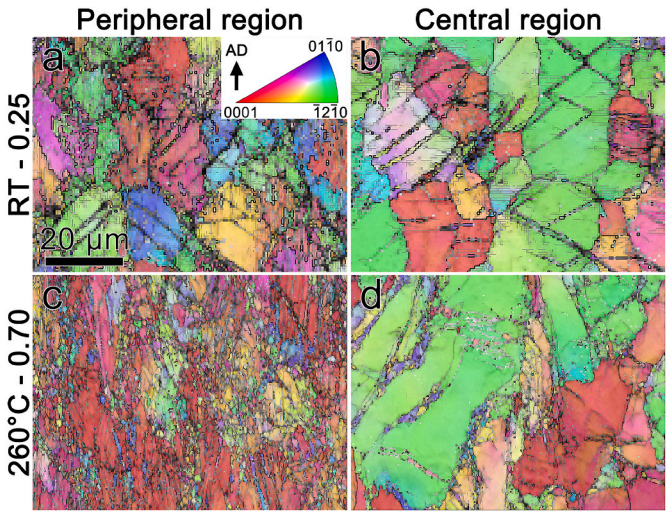

Fig. 9. Inverse pole figure EBSD maps viewed on RD planes of the RS AZ80 Mg alloy rods: The (a) peripheral and (b) central regions of the RT-0.25 sample; The (c) peripheral and (d) central regions of the 260°C-0.70 sample.

than the periphery, as shown in Fig. 12. Both thick twin bands and dislocation walls are seen inside the CGs. Therefore, the EBSD map shown in Fig. 9b is comparable to the TEM image in Fig. 12. In addition, the hardness at the center is significantly lower than at the periphery, as shown in Fig. 2. All these results proves that there is a strain gradient from the periphery to the center, and the actual strain at the center is much lower than the periphery.

As shown in Fig. 13a, the peripheral region of the 260°C-0.70 sample possesses a hierarchical microstructure. The shapes and sizes of the grains vary significantly in the local area. There are equiaxed UFGs formed by recrystallization. There are elongated grains with straight GBs inherited from deformation twins. There are remaining CGs containing high densities of nano-precipitates. Fig. 13b shows the microstructure of the central region of the 260°C-0.70 sample. Similar to the peripheral region, there is also a mixture of equiaxed UFGs, elongated grains, CGs and nano-precipitates. However, some of the elongated grains have wavy GBs, because DRX occurred at these GBs.

Fig. 9c shows that the peripheral region of the 260°C-0.70 sample has the highest density of UFGs. Fig. 14a reveals the details of the UFGs. The majority of the UFGs has sizes smaller than 200 nm, as indicated by the red arrows in Fig. 14a. The β-$Mg_{17}Al_{12}$ nano-precipitates marked by blue arrows are located at boundaries of UFGs. Fig. 14b is a high magnification image showing series of nano-precipitates formed along

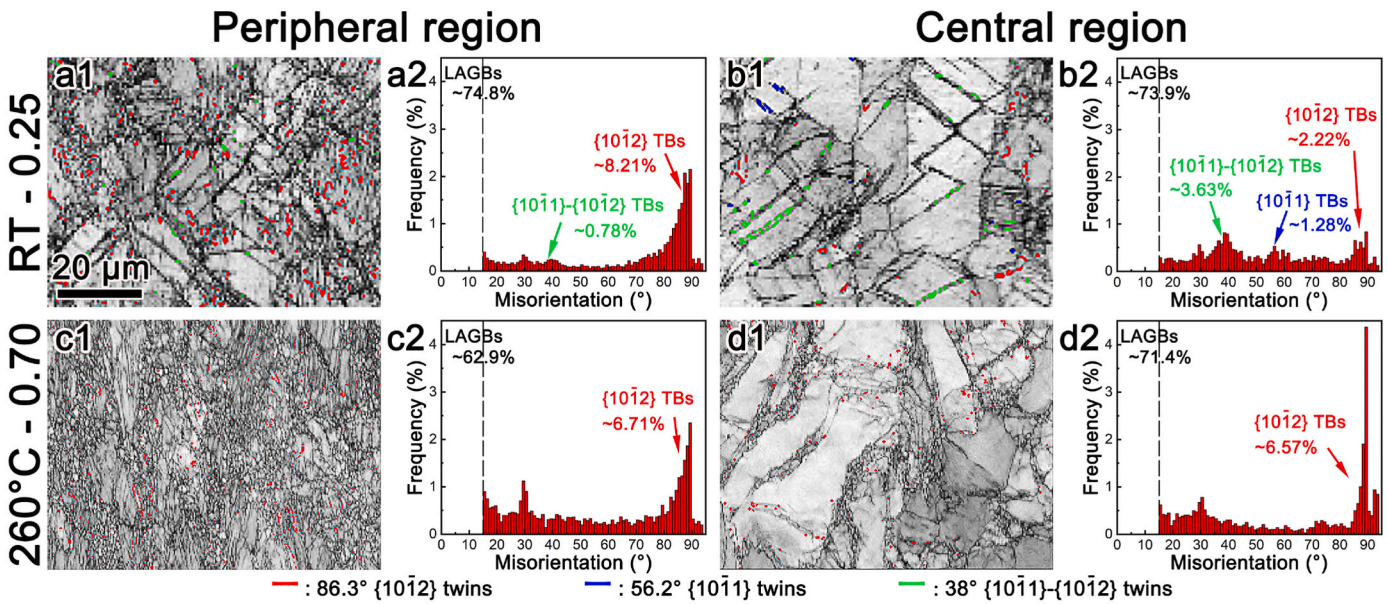

Fig. 10. EBSD maps showing boundaries of different misorientations on the RD planes: Boundaries observed at (a1) the peripheral and (b1) central regions of the RT-0.25 sample, and (a2 and b2) the corresponding statistical distributions of boundary misorientations; Boundaries observed at (c1) the peripheral and (d1) central regions of the 260°C-0.70 sample, and (c2 and d2) the corresponding statistical distributions of boundary misorientations.

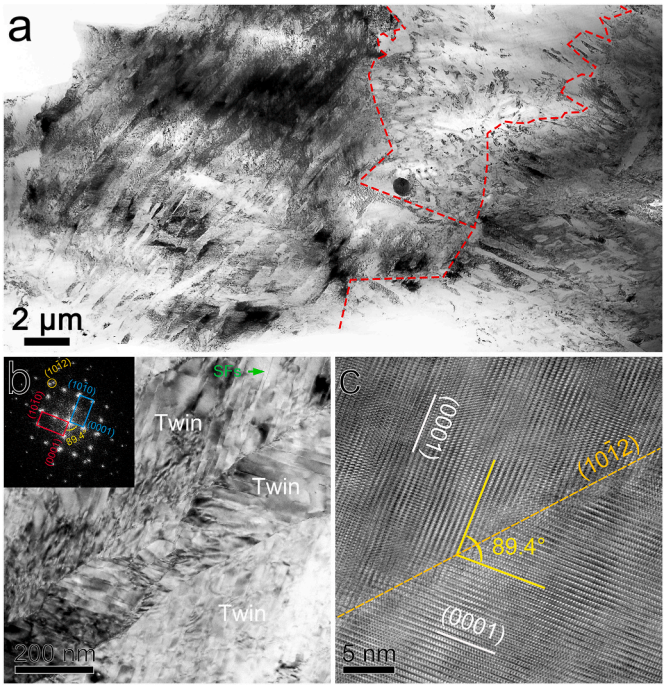

Fig. 11. TEM images showing microstructures at the peripheral region of the RT-0.25 sample: (a) A low magnification bright-field TEM image showing a complex microstructure (the red dashed-lines delineate the GBs inherited from the original CGs); (b) A TEM image showing the {10 $\bar{1}$ 2} twin and an inset of selected area diffraction pattern; (c) A HRTEM image taken at the [1$\bar{2}$ 10] zone axis to show a {10$\bar{1}$ 2} twin boundary.

GBs. The area enclosed by a yellow ellipse has a fragment of the GB pinned by two nano-precipitates. Knowing that DRX occurred in the twin bands during plastic deformation [53], precipitations perhaps occurred simultaneously to compete for heterogeneous nucleation sites such as dislocation boundaries and TBs. High densities of nano-precipitates are effective in inhibiting grain growth by pinning GBs

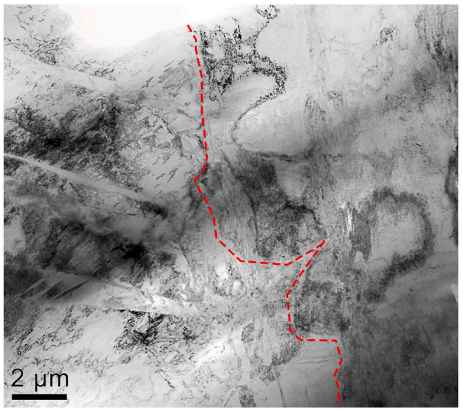

Fig. 12. A bright-field TEM image taken from the central region of the RT-0.25 sample. The red dashed-line delineates the GBs inherited from the original CGs.

and thus suppressing GB migration [55]. Hence a stable mixture of UFGs and nano-precipitates formed in the 260°C-0.70 sample as shown in Figs. 9c and 14a.

Fig. 14c and d shows high densities of β-$Mg_{17}Al_{12}$ nano-precipitates at the CG interiors in peripheral and central regions of the 260°C-0.70 sample, respectively. The nano-precipitates shown in Fig. 14d all have the shapes of short rods. In contrast, the nano-precipitates shown in Fig. 14c are more spherical. In other words, the nano-precipitates formed in the peripheral region have smaller aspect ratios than those formed in the central region.

A grain at the periphery of the 260°C-0.70 sample was orientated to different two-beam conditions for identification of dislocations. Basal <a> dislocations (marked by green arrows) and pyramidal <c + a> dislocations (marked by red arrows) are visible in Fig. 15a. Non-basal <c> dislocations (marked by yellow arrows) and pyramidal <c + a> dislocations are visible in Fig. 15b. There are some I1 SFs connected to <c> dislocations, suggesting that decomposition of the pyramidal <c + a> dislocations has occurred [16].

Fig. 16 presents the XRD patterns of the as-received, RT-0.25 and 260°C-0.70 samples. There are more diffraction peaks of the β-$Mg_{17}Al_{12}$

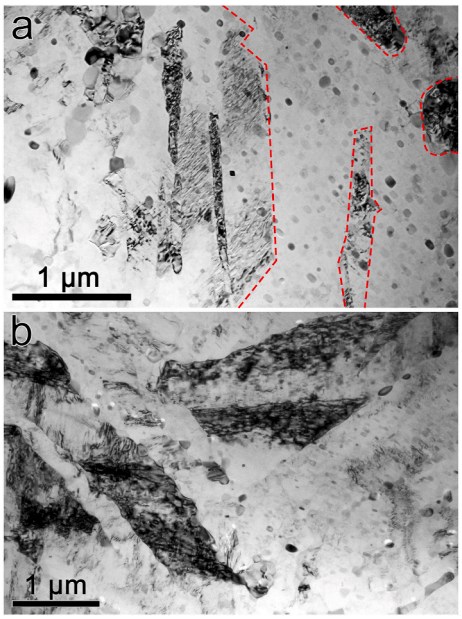

Fig. 13. Bright-field TEM images taken from the (a) peripheral and (b) central regions of the 260°C-0.70 sample. The red dashed-lines mark GBs.

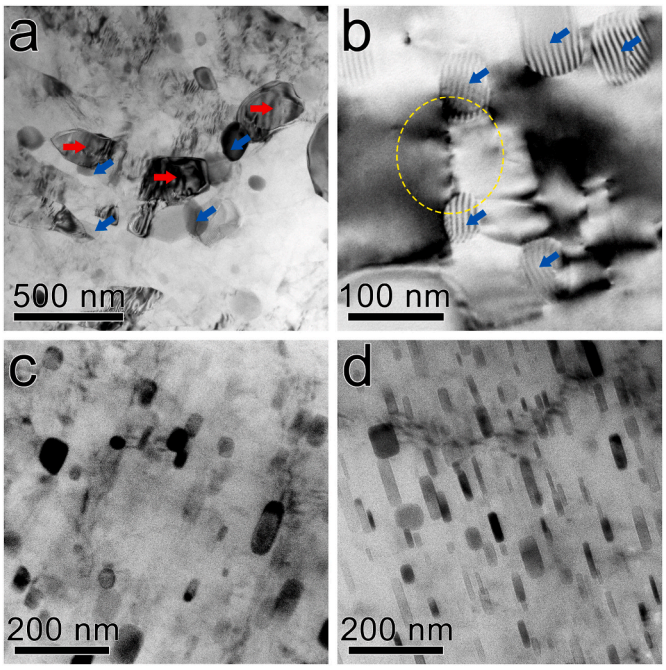

Fig. 14. (a and b) Bright-field TEM images showing UFGs and precipitates in the peripheral region of the 260°C-0.70 sample (recrystallized UFGs and β-$Mg_{17}Al_{12}$ precipitates are marked by red and blue arrows, respectively). Bright-field TEM images showing β-$Mg_{17}Al_{12}$ nano-precipitates at the (c) peripheral and (d) central region of the 260°C-0.70 sample.

phase in the 260°C-0.70 sample than in the as-received and RT-0.25 samples, suggesting that the RS process at 260 °C has caused pronounced precipitation in different orientations. The three samples show different relative peak intensities, suggesting that texture evolutions occurred as a result of RS. This result indicates that high-temperature plastic deformation has driven significant numbers of Al atoms out of the Mg grains for precipitations or segregation to GBs [55,56].

3.4. Fracture of RS AZ80 alloys

Tensile specimens were taken from the peripheral and central regions of the RT-0.25 and 260°C-0.70 samples. As shown in Fig. 17, the fracture surfaces observed from the peripheral and central regions of the RT-0.25 sample are alike, presenting features of brittle failure: (a) cleavage facets and steps are all over the fracture surfaces; (b) some shallow dimples are found beneath edges of steps. The cavity seen at the GB in Fig. 6c and the many large cleavage facets in Fig. 17, suggest that intergranular fractures at GBs and TBs are the major cause of failure.

Both deep dimples (Fig. 18a) and cleavage facets (Fig. 18b) are pronounced on the fracture surface of the 260°C-0.70 sample. In addition, there are high densities of small dimples on the cleavage facets, as shown in Fig. 18b. The mixture of dimples and cleavage facets is attributed to the ductile failure of the bimodal grain structure in the 260°C-0.70 sample. In contrast, tensile specimen taken from the central region of the 260°C-0.70 sample show shallow dimples (Fig. 18c) and large flat areas (Fig. 18d). It is apparent that ductile fracture of CGs is the major failure mechanism at the central region of the 260°C-0.70 sample.

4. Discussions

4.1. Strength calculation

As shown in Fig. 3, both the periphery and center of the 260°C-0.70 sample show excellent combinations of strength and ductility. This has been attributed to the nano-structural hierarchy processed by warm RS. According to Fig. 9c and d, Fig. 13, Figs. 14 and 15, the nano-structural hierarchy consists of bimodal grain size, nano-precipitates (dispersed in grain interiors and GBs) and dislocation structures. Thus, the YS (σ_y) can be estimated by summation of strength increments from GB-strengthening (σ_{GB}), precipitation strengthening (σ_{Orowan}) and dislocation strengthening (σ_{dis}) as [57,58]:

$$\sigma_y = \sigma_{GB} + \sigma_{Orowan} + \sigma_{dis} \quad (1)$$

The GB-strengthening increment is usually calculated by the empirical Hall-Petch equation [59]:

$$\sigma_{GB} = \sigma_0 + kd^{-1/2} \quad (2)$$

where σ_0 is the intrinsic lattice friction stress and k is the Hall-Petch constant; Both of the parameters are texture and grain size dependent in HCP structures [59,60]; d is the average grain size. Statistical analysis based on EBSD and TEM data gives that the average UFG size and CG size at the periphery of 260°C-0.70 sample are 194 nm and 10 μm, respectively; The average UFG size and CG size at the center of 260°C-0.70 sample are 295 nm and 11 μm, respectively. According to literatures [28,59], the fine grains (<2 μm) formed under severe plastic deformation usually possess a strong basal texture, therefore σ_0=21 MPa and k=92 MPa·$\mu m^{1/2}$ are adopted from a fine-grained Mg alloy with similar compositions and texture. The CGs have a comparatively weak texture, therefore σ_0=124 MPa and k=205 MPa·$\mu m^{1/2}$ are adopted due to strong influence of non-basal slip [59,61]. The rule of mixture [61] is used to deduce the overall GB-strengthening increment as:

$$\sigma_{m-GB} = \sigma_{UFG} \times V_{UFG} + \sigma_{CG} \times V_{CG} \quad (3)$$

where σ_{UFG} and σ_{CG} are strength increments contributed by UFGs and CGs, respectively; V_{UFG} and V_{CG} are volume fractions of UFGs and CGs, respectively. The volume fractions of UFGs and CGs are deduced from the EBSD data. The V_{UFG} and V_{CG} at the periphery are 17% and 83%, respectively. The V_{UFG} and V_{CG} at the center are 5% and 95%, respectively. Hence the overall GB-strengthening increments for the peripheral and central regions of the 260°C-0.70 sample are estimated to be 195.3 MPa and 186 MPa, respectively.

The precipitation strengthening increments are mainly attributed to the nano-precipitates dispersed at grain interiors. Therefore, the Orowan

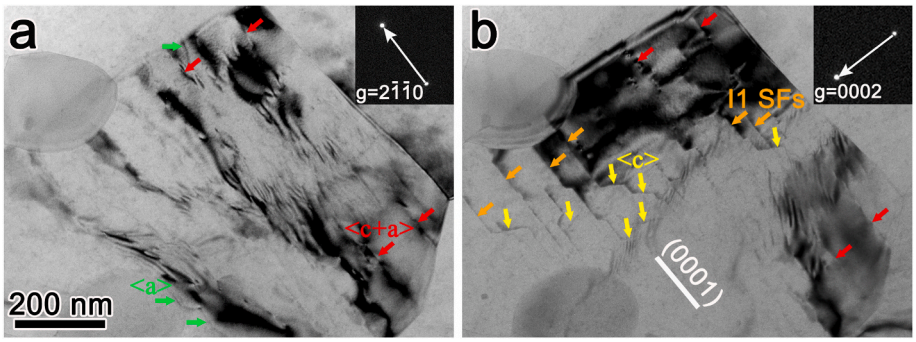

Fig. 15. TEM images in two-beam conditions showing dislocations in the peripheral region of the 260°C-0.70 sample: (a) **g** = 2 $\overline{11}$ 0 and (b) **g** = 0002. The white straight line is parallel to the (0001) basal plane. SFs, <a>, <c> and <c + a> dislocations are marked by orange, green, yellow and red arrows respectively.

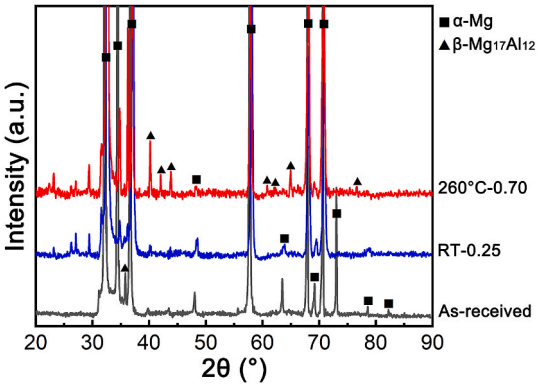

Fig. 16. The XRD patterns of the as-received, RT-0.25 and 260°C-0.70 samples.

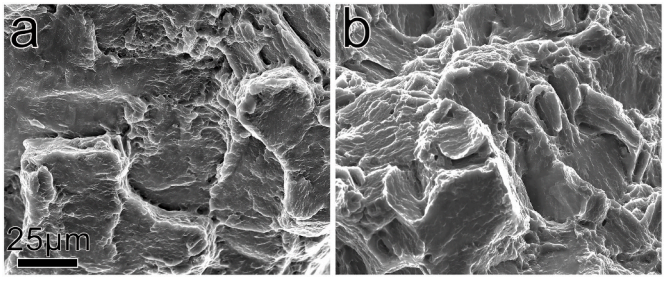

Fig. 17. SEM images showing the fracture surfaces of the (a) peripheral and (b) central regions of the RT-0.25 sample.

equation is adopted for the calculation [62]:

$$\sigma_{Orowan} = \frac{MGb}{2\pi(1-\nu)^{\frac{1}{2}}}\left(\frac{1}{\lambda}\right)\ln\left(\frac{D}{r_0}\right) \tag{4}$$

where M is the Taylor factor, which is estimated from the EBSD data as 2.5; G=1.66×10^4 MPa is the shear modulus, $\boldsymbol{b}$=0.32 nm is the Burgers vector for basal slip, ν=0.3 is Poisson's ratio, D is the mean particle diameter, λ is the effective inter-particle spacing, r_0 is the dislocation core radius which is considered equal to b. The D and λ values are statistically measured from TEM images. The D and λ values measured at the peripheral region of the 260°C-0.70 sample are ~45 nm and ~115 nm, respectively; The D and λ values at the central region are ~28 nm and ~101 nm, respectively. Hence, the precipitation strengthening increments for the peripheral and central regions of the 260°C-0.70 sample are 107.5 MPa and 110.6 MPa, respectively.

The dislocation strengthening increments can be calculated by the Bailey–Hirsch equation [63]:

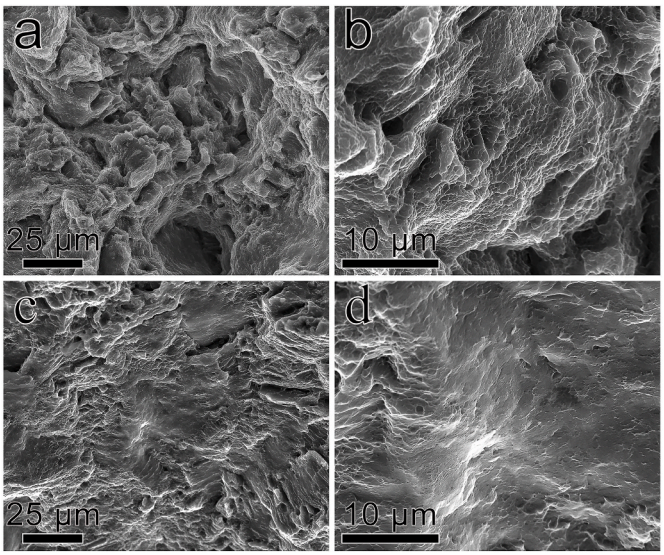

Fig. 18. SEM images showing the fracture surfaces of the (a and b) peripheral and (c and d) central regions of the 260°C-0.70 sample.

$$\sigma_{dis} = M\alpha Gb\sqrt{\rho} \tag{5}$$

where α=0.2 is a temperature dependent constant; ρ is the total dislocation density which consists of statistical and geometrically necessary dislocations (GNDs). In severely deformed metals, the number fraction of statistical dislocations is usually very low [22], therefore in the current case the density of GNDs, ρ_{GNDs}, is considered a rough estimation of the total dislocation density. EBSD data was used for calculating dislocation densities by:

$$\rho_{GNDs} = \frac{2\theta_{KAM}}{xb} \approx \rho \tag{6}$$

where θ_{KAM} is the kernel average misorientation, x is unit length; Both parameters can be deduced from EBSD data. Hence, the dislocation strengthening increments at the peripheral and central regions of the 260°C-0.70 sample are ~54.2 MPa and ~48.9 MPa.

The calculated YS for the peripheral and central regions of the 260°C-0.70 sample are ~357 MPa and ~345.5 MPa, respectively, which are slightly smaller than the tensile test results (388 MPa and 363 MPa). All abovementioned results are collected in Table 3. The discrepancies between experimental test and empirical calculation are mainly attributed to the uncertainties for the parameters used. However, the calculated strength increments do give us some useful hints for explaining the strengthening mechanisms.

Table 3
Strength and strengthening increments for the 260°C-0.70 sample. (The test YS $\sigma_{y.test}$ are obtained by tensile tests; The calculated YS $\sigma_{y.cal}$ are estimated by empirical equations. All the values are in MPa).

Sample	$\sigma_{y.test}$	$\sigma_{y.cal}$	σ_{m-GB}	σ_{Orowan}	σ_{dis}
Peripheral region	388	357	195.3	107.5	54.2
Central region	363	345.5	186	110.6	48.9

4.2. Strengthening mechanisms

According to Table 3 and the microstructural characterization results, the peripheral region possesses smaller average grain sizes, higher dislocation densities and larger inter-particle spacing than the central region. Therefore, the peripheral region shows higher GB-strengthening and dislocation strengthening increments, but lower precipitation strengthening increments than the central region. GBs and dislocations are fast paths for diffusion and preferred sites for heterogeneous precipitation [64,65]. The peripheral region with more UFGs and a higher dislocation density than the central region, tend to have a lower density of nano-precipitates due accelerated coarsening of precipitates. The 260°C-0.70 sample has been processed at elevated temperature; therefore, the dislocation densities are comparatively low throughout the entire sample, thus dislocations strengthening effect is moderate and similar at both peripheral and central regions. Therefore, the main difference in strengthening effect comes from the GB-strengthening increments.

It is widely known that grain refinement in the micrometer range can simultaneously improve strength and ductility for Mg alloys. For example, Wei et al. [16] reported that when the average grain size of a pure Mg decreased from 125 μm to 5.5 μm, its YS increased from 67.7 MPa to 93.8 MPa, and its UL increased from 5.3% to 18.3%. This is because grain refinement to the lower bound of the micrometer range can effectively activate non-basal <c + a> dislocation slip and suppress deformation twinning [17]. However, when the grain size is reduced to ultrafine and nanocrystalline regime, the ductility tends to decrease while the strength still increases [28]. This is because UFGs and nanograins have insufficient space for dislocation propagation and interactions, and thus the strain hardening capabilities of the ultrafine grained materials decrease, resulting in lowered ductility [66].

In this work, the 260°C-0.70 sample possesses bimodal grain size at both peripheral and central regions, as shown in Fig. 9c and d, 13 and 14a. The UFGs provide high strength but lowered ductility. The CGs with an average grain size of ~10 μm provide sufficient space for dislocation accumulations and thus are the major contributor for ductility. During tensile tests, the strong UFG region experiences higher stress and lower strain, in contrast the ductile CG region experiences lower stress and higher strain, thus creating the mechanical incompatibility [67,68]. The mechanical incompatibility in turn stimulates HDI strengthening effect which in the current case is realized by high densities of dislocations in CGs [68,69]. According to the EBSD measurement and as shown in Fig. 9c, the peripheral region has 17 % UFGs in volume fraction which is much higher than the central region. However, the peripheral region has a UL of 8.2% which is even higher than that of the central region. Provided that UFGs alone deteriorate ductility [28], the unique combination of bimodal grain size distribution and the corresponding HDI strengthening effect are the key for the improved strength-ductility synergy.

4.3. Grain refinement mechanisms

Under RS deformation at room temperature, the dominant grain refinement mechanism for the AZ80 Mg alloy rod is deformation twinning as shown in Fig. 11. Deformation twinning can form high densities of TBs to effectively subdivide the CGs as shown in Fig. 11a. Therefore, the RT-0.25 sample is significantly strengthened as shown in Fig. 3a and Table 2. However, the ductility of the RT-0.25 sample was also reduced dramatically to be less than 2.5% elongation, as shown in Table 2. This is because (1) the preferred basal <a> slip alone is unable to provide five independent slip systems for uniform deformation [57], (2) deformation twins with many variances are activated to accommodate the shear strain in the c-axis direction, but in the meantime high stress concentrations are created at twin tips and twin-twin intersections to initiate cracks [57,70–72], and (3) pronounced basal slip in the softly oriented twins (Fig. 11b and c) can cause severe stress concentration and deformation incompatibility at the coherent TBs to initiate cracks [73].

As the deformation temperature increases, the CRSS for non-basal <c + a> dislocation slip can be reduced [53,74], therefore pronounced <c + a> slip can compete with deformation twinning for strain accommodation, as shown in Fig. 15; Moreover, during high temperature deformation, vigorous dislocation activities and double twinning tend to be localized within the primary twins, leading to DRX [53,57], as shown in Fig. 9c and d, Fig. 10c1-d1, and Fig. 13. In such way, deformation twinning in whole CGs are suppressed, instead, localized grain refinement via double twinning and DRX takes dominance [55,57,75,76], resulting in the bimodal grain size distribution in the 260°C-0.70 sample, as shown in Fig. 9c and d and Fig. 10c1-d1.

4.4. Nano-structural hierarchy

The pre-existing precipitates and the saturated solid solution in the as-received AZ80 Mg alloy complicate the microstructural evolution, and result in the nano-structural hierarchy. The precipitates are stable at room temperature; therefore, the shapes and distributions of precipitates are almost identical in the as-received (Fig. 5) and RT-0.25 sample (Fig. 6), despite of the plastic strain of 0.25 and the pronounced twinning and dislocation activities as shown in Figs. 11 and 12. However, as the deformation temperature was risen to 260 °C, the solubility of Al in Mg was increased. Meanwhile, under the effect of stress driven dislocation and twinning activities, the pre-existing precipitates were fragmented and partially dissolved back into the Mg matrix via pipe diffusion [77] and dislocation shearing mechanism [78]; During the water-cooling process, Al atoms precipitate out again at defects such as dislocations and GBs [55,79], resulting in the re-distribution of β-$Mg_{17}Al_{12}$ precipitates as shown in Fig. 7. As shown in Fig. 14, nano-precipitates formed in both UFG and CG regions. According to literatures [80,81], precipitates can pose strong pinning effects against dislocation slip and GB-migration, thus limiting grain growth during DRX in the UFG region, thus stabilized the UFG structures, as shown in Fig. 14a. In CGs, the shape and density of nano-precipitates are affected by plastic strain and dislocation density. During RS, the impact strain transmits from the periphery to the interior. Thus, the dislocation density at the periphery is higher than the center. During the repetitive 260°C-swaging and cooling process, the dislocation lines serve as fast diffusion paths for the solute atoms in the matrix to rapidly diffuse to the pre-existing or early formed precipitates [25]; Small precipitates may merge with the neighboring large precipitate, thus the large precipitates can grow at the expense of the small precipitates; Severe local shear may bring some well-separated precipitates closer and thus promote their coalescence [82]. Via the abovementioned plastic strain assisted growth and coalescence mechanisms, nano-precipitates in the metastable rod shapes tend to disappear and the remaining precipitates can grow into stable spherical shapes. Therefore, at the peripheral region, where the plastic strain is higher, the β-$Mg_{17}Al_{12}$ precipitates are more spherical, larger and located further apart (Figs. 13a and 14c), and in contrast, at the central region, where the plastic strain is lower, the β-$Mg_{17}Al_{12}$ precipitates are mostly rod shapes, smaller and located closer (Fig. 14d).

In addition to the bimodal grain size distribution, high densities of nano-precipitates formed at GBs of the UFGs and at CG interiors, resulted in the nano-structural hierarchy as shown in Fig. 13a. As mentioned earlier, the bimodal grain size distributions stimulate the HDI strengthening effect [67,83]. Provided that the nano-precipitates in CGs

exert pinning effects to dislocations, as the GND densities increase under the effect of back-stress [84,85], the CG regions can possess very high strain hardening rate to help sustaining ductility [86]. The nano-precipitates at GBs poses negligible dislocation pinning effect, but they can help increase the stability and strength of GBs against dislocation pile-up [87,88], and thus improve the overall GB-strengthening effect. To sum up, the nano-structural hierarchy improves the strength-ductility synergy by adjusting the HDI strengthening effect. Thus, nano-structural hierarchy design is considered an economical option for mechanical properties optimizations in supersaturated light-weight alloys such as Mg alloys, Ti alloys and Al alloys [89].

5. Conclusions

In this work, RS at room temperature and elevated temperature have been done to process the AZ80 Mg alloy with improved mechanical properties. Based on extensive experimental work and theoretical analysis, four conclusions can be drawn as follows.

1. Both RT-0.25 sample processed by room temperature RS and 260°C-0.70 sample processed by high temperature RS show gradient hardness distributions from peripheries to the centers of the rods. Despite of similar hardness distributions and yield strengths, the two samples show completely different microstructures and ductility.
2. The microstructures and tensile properties at the peripheral and central regions of the RT-0.25 sample were characterized separately. The periphery of the sample has a very high density of deformation twins in most of the grains and some cracked large precipitates, resulting in high YS but negligible ductility. The center of the sample has a twin density lower than that at the periphery and some cavities at GBs and precipitates, resulting in slightly lower YS and higher ductility than the periphery.
3. The microstructures and tensile properties at the peripheral and central regions of the 260°C-0.70 sample were also characterized separately. For the peripheral region, the YS is 388 MPa which is 78.8% higher than the as-received sample; The UTS is 471 MPa, which is 30.5% higher; The UL is 8.2%. For the central region, the YS, UTS and UL are 363 MPa, 427 MPa, 7.0%, respectively. The improved combinations of strength and ductility at both the peripheral and central regions of the 260°C-0.70 sample are attributed to the nano-structural hierarchy consists of bimodal grain size distributions and high densities of nano-precipitates located at GBs of the UFGs and at CG interiors.
4. Repetitive conduct of 260°C-swaging and water cooling can promote $<c+a>$ dislocation slip and localized grain refinement via twinning and DRX, and thus to restrict the total area fraction of deformation twins. This processing route can also change the precipitation kinetics under the effect of plastic strain, resulting in spherical nano-precipitates of lower densities at the periphery and rod-like nano-precipitates of higher densities at the center.

Declaration of competing interest

The authors declare that they have no known competing financial interests or personal relationships that could have appeared to influence the work reported in this paper.

Acknowledgments

This research is funded by the National Key R&D Program of China (Grant No. 2021YFA1200203), the National Natural Science Foundation of China (Grant Nos. 51971112 and 52071181), the Six Talent Peaks Project of Jiangsu Province (Grant No. 2017-XCL-051), and Jiangsu Province Leading Edge Technology Basic Research Major Project (BK20222014). The authors also want to acknowledge the support of the Jiangsu Key Laboratory of Advanced Micro-Nano Materials and Technology. The authors are thankful for the technical support from the Materials Characterization Facility of Nanjing University of Science and Technology.

References

[1] Yang Y, Xiong X, Chen J, Peng X, Chen D, Pan F. Research advances of magnesium and magnesium alloys worldwide in 2022. J Magnesium Alloys 2023;11:2611–54.
[2] Li Y, Zhang A, Li C, Xie H, Jiang B, Dong Z, et al. Recent advances of high strength Mg-RE alloys: alloy development, forming and application. J Mater Res Technol 2023;26:2919–40.
[3] Li L, Gao B, Wei K, Hu Z, Yu Y, Sun WW, et al. Improved impact toughness of laminate heterogeneous AZ31/GW103K alloys by interface delamination. Mater Sci Eng, A 2023;871:144882.
[4] Wu ZX, Ahmad R, Yin B, Sandlöbes S, Curtin WA. Mechanistic origin and prediction of enhanced ductility in magnesium alloys. Science 2018;359:447–52.
[5] Xu W, Birbilis N, Sha G, Wang Y, Daniels JE, Xiao Y, et al. A high-specific-strength and corrosion-resistant magnesium alloy. Nat Mater 2015;14:1229–35.
[6] Zhang X, Zhou R, Li C, Guo S, Yue H. A visco-plastic self-consistent analysis of the compression anisotropy in extruded rare earth magnesium alloy. J Mater Res Technol 2024;29:2154–65.
[7] Proust G. Processing magnesium at room temperature. Science 2019;365:30–1.
[8] Dai Y, Yi Q, Hu Y, Jiang B, Pan F. The discrepancy in basal slip hardening rates of cast and extruded Mg-Y-Zr alloys. J Mater Res Technol 2024;28:4275–88.
[9] Tang S, Kou Z, Xin T, Zhang Z, Feng T, Luo T, et al. Achieving high strength via solutes co-clustering and solvents redistribution in an ultralightweight BCC magnesium alloy. Mater Res Lett 2023;11(7):556–62.
[10] Shi Q, Natarajan AR, Van der Ven A, Allison J. Partitioning of Ca to metastable precipitates in a Mg-rare earth alloy. Mater Res Lett 2022;11(3):222–30.
[11] Hua ZM, Zha M, Meng ZY, Jin SB, Sha G, Wang TS, et al. Rapid dislocation-mediated solute repartitioning towards strain-aging hardening in a fine-grained dilute magnesium alloy. Mater Res Lett 2022;10(1):21–8.
[12] Kula A, Jia X, Mishra RK, Niewczas M. Strain rate sensitivity of binary Mg-Gd and Mg-Y solid solutions. Int J Plast 2022;155:103321.
[13] Fan M, Zhang Z, Cui Y, Liu L, Liu Y, Liaw PK. Achieving strength and ductility synergy via a nanoscale superlattice precipitate in a cast Mg-Y-Zn-Er alloy. Int J Plast 2023;163:103558.
[14] Xu M, Li N, Sha X, Liu Y, Gao B, Xiao L, et al. In-situ TEM observations on interaction of basal <a> dislocations and β′ phases in a Mg-Gd binary alloy. Mater Sci Eng, A 2022;841:143017.
[15] Liu H, Huang H, Yang X, Li C, Yan J, Jiang J, et al. Microstructure and mechanical property of a high-strength Mg-10Gd-6Y-1.5Zn-0.5Zr alloy prepared by multi-pass equal channel angular pressing. J Magnesium Alloys 2017;5:231–7.
[16] Wei K, Hu R, Yin D, Xiao L, Pang S, Cao Y, et al. Grain size effect on tensile properties and slip systems of pure magnesium. Acta Mater 2021;206:116604.
[17] Luo X, Feng Z, Yu T, Luo J, Huang T, Wu G, et al. Transitions in mechanical behavior and in deformation mechanisms enhance the strength and ductility of Mg-3Gd. Acta Mater 2020;183:398–407.
[18] Wu G, Chan KC, Zhu L, Sun L, Lu J. Dual-phase nanostructuring as a route to high-strength magnesium alloys. Nature 2017;545:80–3.
[19] Edalati K, Bachmaier A, Beloshenko VA, Beygelzimer Y, Blank VD, Botta WJ, et al. Nanomaterials by severe plastic deformation: review of historical developments and recent advances. Mater Res Lett 2022;10(4):163–256.
[20] Peng P, Xue H, She J, Zhang J, Tang A, Long S, et al. Ultrafine-grained Mg alloy: preparation, properties, design strategy. J Mater Res Technol 2024;29:4480–504.
[21] Rezaei A, Mahmudi R, Cayron C, Logé RE. Simple shear extrusion versus equal channel angular pressing: a comparative study on the microstructure and mechanical properties of an Mg alloy. J Magnesium Alloys 2023;11:1769–90.
[22] Liu Y, Cao Y, Mao Q, Zhou H, Zhao Y, Jiang W, et al. Critical microstructures and defects in heterostructured materials and their effects on mechanical properties. Acta Mater 2020;189:129–44.
[23] Xu D, Wang M, Li T, Wei X, Lu Y. A critical review of the mechanical properties of CoCrNi-based medium-entropy alloys. Microstructures 2022;2:2022001.
[24] Wang T, Zha M, Du C, Jia HL, Wang C, Guan K, et al. High strength and high ductility achieved in a heterogeneous lamella-structured magnesium alloy. Mater Res Lett 2023;11(3):187–95.
[25] Zha M, Ma X, Jia HL, Hua ZM, Fan ZX, Yang ZZ, et al. Dynamic precipitation and deformation behaviors of a bimodal-grained WE43 alloy with enhanced mechanical properties. Int J Plast 2023;167:103682.
[26] Fan J, Ji X, Fu L, Wang J, Ma S, Sun Y, et al. Achieving exceptional strength-ductility synergy in a complex-concentrated alloy via architected heterogeneous grains and nano-sized precipitates. Int J Plast 2022;157:103398.
[27] Nie J, Chen Y, Song L, Fan Y, Cao Y, Xie K, et al. Enhancing strength and ductility of Al-matrix composite via a dual-heterostructure strategy. Int J Plast 2023;171:103825.
[28] Wan Y, Tang B, Gao Y, Tang L, Sha G, Zhang B, et al. Bulk nanocrystalline high-strength magnesium alloys prepared via rotary swaging. Acta Mater 2020;200:274–86.
[29] Cui X, Liu W, Yang Y, Zhang Y, Li R, Wei G, et al. High-strength Mg-6Li-3Al-0.4Ce alloy fabricated by rotary swaging. Scripta Mater 2024;243:115954.
[30] Mao Q, Liu Y, Zhao YH. A review on mechanical properties and microstructure of ultrafine grained metals and alloys processed by rotary swaging. J Alloys Compd 2022;896:163122.

[31] Chen X, Liu C, Wan Y, Jiang S, Han X, Chen Z. Formation of nanocrystalline AZ31B Mg alloys via cryogenic rotary swaging. J Magnesium Alloys 2023;11:1580–91.
[32] Yi Q, Dai Y, Hu Y, Jiang B, Pan F. Nanocrystallization and strengthening of Mg-Dy-Zr alloys by room temperature rotary swaging. J Mater Res Technol 2024;30:6777–86.
[33] Chen H, Yang Y, Hu F, Liu X, Kong F, Cui X, et al. Improvement of severe plastic deformation realized by several passes rotary swaging in the microstructure and properties of Mg-0.6Mn-0.5Al-0.5Zn-0.4Ca alloy. Mater Sci Eng, A 2023;865:144629.
[34] Yang Y, Chen X, Nie J, Wei K, Mao Q, Lu F, et al. Achieving ultra-strong Magnesium-lithium alloys by low-strain rotary swaging. Mater Res Lett 2021;9(6):255–62.
[35] Zhou G, Yang Y, Luo Y, Li Q, Luo Q, Zhang Y, et al. Synergistic improvement of strength and plasticity of Mg-6Li-3Al-1Sn alloy by microstructure regulation via rotary swaging. Mater Res Lett 2023;11(12):1031–9.
[36] Fadaei A, Farahafshan F, Sepahi-Boroujeni S. Spiral equal channel angular extrusion (Sp-ECAE) as a modified ECAE process. Mater Des 2017;113:361–8.
[37] Jin SC, Cha JW, Go J, Bae JH, Park SH. Comparative study of extrudability, microstructure, and mechanical properties of AZ80 and BA53 alloys. J Magnesium Alloys 2023;11:249–58.
[38] Jung JG, Park SH, Yu H, Kim YM, Lee YK, You BS. Improved mechanical properties of Mg-7.6Al-0.4Zn alloy through aging prior to extrusion. Scripta Mater 2014;93:8–11.
[39] Kim HJ, Kim YJ, Park SH. Acceleration of aging behavior and improvement of mechanical properties of extruded AZ80 alloy through (10–12) twinning. J Magnesium Alloys 2023;11:671–83.
[40] Lee GM, Lee JU, Park SH. Effects of post-heat treatment on microstructure, tensile properties, and bending properties of extruded AZ80 alloy. J Mater Res Technol 2021;12:1039–50.
[41] Luo L, Xiao Z, Huo Q, Yang Y, Huang W, Guo J, et al. Enhanced mechanical properties of a hot-extruded AZ80 Mg alloy rod by pre-treatments and post-hot compression. J Alloys Compd 2018;740:180–93.
[42] Sepahi-Boroujeni S, Sepahi-Boroujeni A. Improvements in microstructure and mechanical properties of AZ80 magnesium alloy by means of an efficient, novel severe plastic deformation process. J Manuf Process 2016;24:71–7.
[43] Shi G, Yuan J, Li T, Zhang K, Li X, Li Y, et al. Enhanced precipitation strengthening of extruded Mg-8 wt.%Al-0.5 wt.%Zn (AZ80) magnesium alloy by extension twinning. Mater Sci Eng, A 2020;774:138906.
[44] Tang L, Zhao Y, Islamgaliev RK, Tsao CYA, Valiev RZ, Lavernia EJ, et al. Enhanced strength and ductility of AZ80 Mg alloys by spray forming and ECAP. Mater Sci Eng, A 2016;670:280–91.
[45] Zhang Z, Yuan L, Shan D, Guo B. The quantitative effects of temperature and cumulative strain on the mechanical properties of hot-extruded AZ80 Mg alloy during multi-directional forging. Mater Sci Eng, A 2021;827:142036.
[46] Zhao X, Gao P, Chen G, Wei J, Zhu Z, Yan F, et al. Effects of aging treatments on low-cycle fatigue behavior of extruded AZ80 for automobile wheel disks. Mater Sci Eng, A 2021;799:140366.
[47] Zhao X, Li S, Zhang Z, Gao P, Kan S, Yan F. Comparisons of microstructure homogeneity, texture and mechanical properties of AZ80 magnesium alloy fabricated by annular channel angular extrusion and backward extrusion. J Magnesium Alloys 2020;8:624–39.
[48] Zhao X, Li SC, Zheng YS, Liu ZR, Chen K, Yu JM, et al. The microstructure evolution, texture weakening mechanism and mechanical properties of AZ80 Mg alloy processed by repetitive upsetting-extrusion with reduced deformation temperature. J Alloys Compd 2021;883:160871.
[49] Zhao X, Yan FF, Zhang ZM, Gao PC, Li SC. Influence of heat treatment on precipitation behavior and mechanical properties of extruded AZ80 magnesium alloy. Acta Metall Sin-Engl 2021;34:54–64.
[50] Zhou X, Zhang J, Chen X, Zhang X, Li M. Fabrication of high-strength AZ80 alloys via multidirectional forging in air with no need of ageing treatment. J Alloys Compd 2019;787:551–9.
[51] Robson JD, Lawson MJ, Donoghue JM, Guo J, Davis AE. Discontinuous precipitation in Mg-Al alloy studied in 3-dimensions. Scripta Mater 2023;227:115265.
[52] Kim HJ, Jo S, Park SH. Improved continuous precipitation kinetics and tensile properties of extruded AZ80 alloy through {10–12} twin formation. J Magnesium Alloys 2023;11:3323–37.
[53] Dogan E, Vaughan MW, Wang SJ, Karaman I, Proust G. Role of starting texture and deformation modes on low-temperature shear formability and shear localization of Mg-3Al-1Zn alloy. Acta Mater 2015;89:408–22.
[54] Sabbaghian M, Fakhar N, Nagy P, Fekete K, Gubicza J. Investigation of shear and tensile mechanical properties of ZK60 Mg alloy sheet processed by rolling and sheet extrusion. Mater Sci Eng, A 2021;828:142098.
[55] Ma XL, Prameela SE, Yi P, Fernandez M, Krywopusk NM, Kecskes LJ, et al. Dynamic precipitation and recrystallization in Mg-9wt.%Al during equal-channel angular extrusion: a comparative study to conventional aging. Acta Mater 2019;172:185–99.
[56] Liu F, Xin R, Zhong Y, Liu Q. Effect of cold rolling on aging precipitation and mechanical properties of magnesium-aluminum alloy. J Magnesium Alloys; 2023. In Press.
[57] Cao Y, Ni S, Liao X, Song M, Zhu Y. Structural evolutions of metallic materials processed by severe plastic deformation. Mater Sci Eng, R 2018;133:1–59.
[58] Valiev RZ. Nanostructural design of superstrong metallic materials by severe plastic deformation processing. Microstructures 2023;3:2023004.
[59] Yuan W, Panigrahi SK, Su JQ, Mishra RS. Influence of grain size and texture on Hall-Petch relationship for a magnesium alloy. Scripta Mater 2011;65:994–7.
[60] Razavi SM, Foley DC, Karaman I, Hartwig KT, Duygulu O, Kecskes LJ, et al. Effect of grain size on prismatic slip in Mg-3Al-1Zn alloy. Scripta Mater 2012;67:439–42.
[61] Pan H, Kang R, Li J, Xie H, Zeng Z, Huang Q, et al. Mechanistic investigation of a low-alloy Mg-Ca-based extrusion alloy with high strength–ductility synergy. Acta Mater 2020;186:278–90.
[62] Fu W, Dang P, Guo S, Ren Z, Fang D, Ding X, et al. Heterogeneous fiberous structured Mg-Zn-Zr alloy with superior strength-ductility synergy. J Mater Sci Technol 2023;134:67–80.
[63] Ma QX, Yang HJ, Wang Z, Shi XH, Liaw PK, Qiao JW. High strength and ductility in partially recrystallized $Fe_{40}Mn_{20}Cr_{20}Ni_{20}$ high-entropy alloys at cryogenic temperature. Microstructures 2022;2:2022015.
[64] Zhang Z, Zhang J, Xie J, Liu S, He Y, Guan K, et al. Developing a low-alloyed fine-grained Mg alloy with high strength-ductility based on dislocation evolution and grain boundary segregation. Scripta Mater 2022;209:114414.
[65] Zhou H, Cheng GM, Ma XL, Xu WZ, Mathaudhu SN, Wang QD, et al. Effect of Ag on interfacial segregation in Mg-Gd-Y-(Ag)-Zr alloy. Acta Mater 2015;95:20–9.
[66] Zhao YH. In situ thermomechanical processing to avoid grain boundary precipitation and strength-ductility loss of age hardening alloys. Trans Nonferrous Metals Soc China 2021;31:1205–16.
[67] Wu XL, Zhu YT. Heterogeneous materials: a new class of materials with unprecedented mechanical properties. Mater Res Lett 2017;5(8):527–32.
[68] Zhu YT, Wu XL. Perspective on hetero-deformation induced (HDI) hardening and back stress. Mater Res Lett 2019;7(10):393–8.
[69] Yang Y, Liu Y, Yan S, Jiang S, He Z, Pan H, et al. On the micromechanism of superior strength and ductility synergy in a heterostructured Mg-2.77Y alloy. J Magnesium Alloys 2024;12:2793–811.
[70] Huang ZW, Jin SB, Zhou H, Li YS, Cao Y, Zhu YT. Evolution of twinning systems and variants during sequential twinning in cryo-rolled titanium. Int J Plast 2019;112:52–67.
[71] Kumar MA, Gong M, Beyerlein IJ, Wang J, Tomé CN. Role of local stresses on co-zone twin-twin junction formation in HCP magnesium. Acta Mater 2019;168:353–61.
[72] Jo S, Lee GM, Lee JU, Kim YM, Park SH. Effect of characteristics and distribution of $Mg_{17}Al_{12}$ precipitates on tensile and bending properties of high-Al-containing Mg alloys. J Magnesium Alloys 2024;12:779–93.
[73] Li FF, Fang G. Stress-state dependency of ductile fracture in an extruded magnesium alloy and its underlying mechanisms. Int J Plast 2022;152:103258.
[74] Wang M, He BB, Huang MX. Strong and ductile Mg alloys developed by dislocation engineering. J Mater Sci Technol 2019;35:394–5.
[75] Tang L, Zhao Y, Liang N, Islamgaliev RK, Valiev RZ, Zhu YT. Localized deformation via multiple twinning in a Mg-Gd-Y-Zr alloy processed by high-pressure torsion. Mater Sci Eng, A 2016;677:68–75.
[76] Peng R, Xu C, Li Y, Zhong S, Cao X, Ding Y. Multiple-twinning induced recrystallization and texture optimization in a differential-temperature-rolled AZ31B magnesium alloy with excellent ductility. Mater Res Lett 2022;10(5):318–26.
[77] Love GR. Dislocation pipe diffusion. Acta Metall 1964;12:731–7.
[78] Bhattacharyya JJ, Wang F, Stanford N, Agnew SR. Slip mode dependency of dislocation shearing and looping of precipitates in Mg alloy WE43. Acta Mater 2018;146:55–62.
[79] Yang Y, Guo J, Wang C, Zhang T, Jiang W, Zhang Z, et al. The effects of deformation parameters and cooling rates on the aging behavior of AZ80+0.4%Ce. J Magnesium Alloys 2024;12:639–58.
[80] Li YK, Zha M, Jia HL, Wang SQ, Zhang HM, Ma X, et al. Tailoring bimodal grain structure of Mg-9Al-1Zn alloy for strength-ductility synergy: Co-regulating effect from coarse Al_2Y and submicron $Mg_{17}Al_{12}$ particles. J Magnesium Alloys 2021;9:1556–66.
[81] Zhang J, Peng P, Yang Q, Luo AA. Bimodal grain structure formation and strengthening mechanisms in Mg-Mn-Al-Ca extrusion alloys. J Magnesium Alloys 2023;11:4407–19.
[82] Sha G, Cerezo A. Kinetic Monte Carlo simulation of clustering in an Al–Zn–Mg–Cu alloy (7050). Acta Mater 2005;53:907–17.
[83] Zha M, Wang SQ, Wang T, Jia HL, Li YK, Hua ZM, et al. Developing high-strength and ductile Mg-Gd-Y-Zn-Zr alloy sheet via bimodal grain structure coupling with heterogeneously-distributed precipitates. Mater Res Lett 2023;11(9):772–80.
[84] Zhu YT, Wu XL. Heterostructured materials. Prog Mater Sci 2023;131:101019.
[85] Zhou T, Li Y, Guo F, Li Q, Jia Z, Liu D. Achieving high strength-ductility synergy in Mg-6Sn-3Zn-0.3Zr (wt.%) alloy via a combination of casting, pre-treatment and hot extrusion. J Magnesium Alloys 2023. In Press.
[86] Ovid'ko IA, Valiev RZ, Zhu YT. Review on superior strength and enhanced ductility of metallic nanomaterials. Prog Mater Sci 2018;94:462–540.
[87] Liu Y, Xu MN, Xiao LR, Chen XF, Hu ZH, Gao B, et al. Dislocation array reflection enhances strain hardening of a dual-phase heterostructured high-entropy alloy. Mater Res Lett 2023;11(8):638–47.
[88] Qi YL, Zhao L, Sun X, Zong HX, Ding XD, Jiang F, et al. Enhanced mechanical performance of grain boundary precipitation-hardened high-entropy alloys via a phase transformation at grain boundaries. J Mater Sci Technol 2021;86:271–84.
[89] Liddicoat PV, Liao XZ, Zhao YH, Zhu YT, Murashkin MY, Lavernia EJ, et al. Nanostructural hierarchy increases the strength of aluminium alloys. Nat Commun 2010;1:63.